Materials Research Bulletin 192 (2025) 113583

Contents lists available at ScienceDirect

Materials Research Bulletin

journal homepage: www.elsevier.com/locate/matresbu

Research Papers

Gas sensing performance of α-, α/β-, and β-Ga_2O_3 polymorphs

Nyepudzai C. Gatsi [a], Murendeni I. Nemufulwi [b], Gugu H. Mhlongo [b,*], Nosipho Moloto [c], Rudolph M. Erasmus [d], Elizabeth Coetsee [e], Hendrik C. Swart [e], Odireleng M. Ntwaeaborwa [f,*]

[a] School of Physics, University of the Witwatersrand, 1 Jan Smuts Avenue, Braamfontein, 2050, South Africa
[b] DSI/CSIR Centre for Nanostructures and Advanced Materials, Council for Scientific and Industrial Research, Pretoria 0001, South Africa
[c] School of Chemistry, University of the Witwatersrand, 1 Jan Smuts Avenue, Braamfontein, 2050, South Africa
[d] School of Physics and Microscopy and Microanalysis Unit, University of the Witwatersrand, Johannesburg, South Africa
[e] Department of Physics, University of the Free State, P.O. Box 339, Bloemfontein, 9300, South Africa
[f] Department of Physical and Earth Sciences, Sol Plaatje University, Kimberley 8300, South Africa

ARTICLE INFO

Keywords:
Gallium oxide
Polymorph
Nanowires
Gas sensing

ABSTRACT

This paper reports the detection of SO_2, NH_3, and CO gases using Ga_2O_3 polymorphs. The α-Ga_2O_3, α/β-Ga_2O_3, and β-Ga_2O_3 sensing materials were prepared using the hydrothermal method, followed by calcination at different temperatures ranging from 550 °C to 950 °C. The gas sensing properties were measured and analyzed based on the polymorphism-induced physicochemical properties of the sensing materials. Different Ga_2O_3 polymorphs showed distinct sensing properties, and factors contributing to this preferential gas detection behavior are discussed in detail. The proposed gas sensing mechanisms were discussed. Notably, the gas sensing performance of the α/β-Ga_2O_3-based sensor is reported here for the first time.

1. Introduction

Many industrial activities that drive economic growth, such as food production, energy generation, and transportation, depend on fossil fuel combustion. This combustion process emits harmful gases that deteriorate air quality and harm the environment [1]. Therefore, achieving sustainable development requires strategies that promote economic growth while reducing environmental harm. One such strategy involves reducing the release of toxic gases into the atmosphere [2], which can be achieved through continuous air quality monitoring.

Among the gases monitored, particular attention is given to hazardous pollutants such as carbon monoxide (CO), sulfur dioxide (SO_2), and ammonia (NH_3), due to their significant impact on human health and the environment [2]. CO is an odorless gas produced by the incomplete combustion of fossil fuels in various industrial and household processes. According to World Health Organization guidelines, exposure to 87.1 ppm CO for 15 min can raise carboxyhemoglobin levels above 2.5 %, leading to neurological disorders, cardiovascular diseases, and even death [3]. Similarly, inhalation of gases such as SO_2 and NH_3 can cause shortness of breath and chronic bronchitis [2]. In addition, these gases are major contributors to the formation of ground-level ozone, acid rain, and photochemical smog, all of which negatively impact the ecosystem [4]. Therefore, there is an urgent need to develop highly sensitive gas-sensing materials for rapid detection of these gases to protect human health and the environment. Among these materials, semiconductor metal oxides (SMOs) are promising candidates due to their excellent chemical stability, low costs, ease of operation, and tunable sensing properties [5].

Due to these advantages, SMOs have been extensively studied for applications in chemiresistive gas sensors. However, to produce a measurable change in resistance when interacting with target gas molecules, most SMO-based sensors require high operating temperatures [6]. This challenge has driven extensive research into strategies for improving gas sensor performance at lower operating temperatures. These strategies include surface modification of SMOs through noble metal decoration, metal-ion doping, heterostructure design, and the optimization of their physicochemical properties [7]. As a result, various SMOs, including ZnO [8], SnO_2 [9], and Ga_2O_3 [10], have been extensively studied for gas sensing applications.

Ga_2O_3, an n-type SMO, offers several key advantages, including excellent catalytic behavior, good chemical and thermal stability, and non-toxicity. In addition, Ga_2O_3 is capable of detecting gases at low

* Corresponding authors.
E-mail addresses: gmhlongo@csir.co.za (G.H. Mhlongo), martin.ntwaeaborwa@spu.ac.za (O.M. Ntwaeaborwa).

https://doi.org/10.1016/j.materresbull.2025.113583
Received 28 August 2024; Received in revised form 21 May 2025; Accepted 27 May 2025
Available online 28 May 2025

concentrations and shows a strong correlation between material composition and gas sensing properties [11,12]. These attributes make Ga_2O_3 a promising material for sensing harmful gases, even in harsh environments. In particular, Ga_2O_3 has been widely used to detect both reducing and oxidizing gases over a broad range of operating temperatures [10,13], owing to the diverse morphologies of the material, which enhance its gas sensing properties [14,15]. However, key challenges include slow response and recovery times, limited selectivity, and high operating temperatures ($\geq$ 700 °C) [10]. These limitations lead to high power consumption, shorter sensor lifespan, and restricted use of other Ga_2O_3 phases, which are stable at lower temperatures. These challenges highlight the need for continued research on Ga_2O_3-based sensors to enhance sensitivity and selectivity at low operating temperatures. Such improvements can be achieved through morphology optimization, microstructural control, and management of incidental impurities.

In its pure form, Ga_2O_3 exists in five different crystalline phases: α-, δ-, γ-, ε(κ)-, and β-Ga_2O_3 [16]. These polymorphs present distinct structural stabilities and Ga-O coordination. For example, α-Ga_2O_3 is stable at calcination temperatures ranging from ~ 400 °C and 600 °C while β-Ga_2O_3 stabilizes at temperatures above 600 °C [17]. β-Ga_2O_3 is preferred for the detection of toxic gases at high operating temperatures due to its high thermal stability [10]. Regarding Ga-O coordination, the rhombohedral α-Ga_2O_3 crystal structure contains Ga atoms surrounded by six O atoms, forming a distorted octahedral coordination geometry [11]. Meanwhile, the monoclinic β-Ga_2O_3 crystal structure contains two non-equivalent Ga sites and three non-equivalent O sites. The Ga(I) and Ga(II) are tetrahedrally and octahedrally coordinated with O, respectively. The distinct O(I) and O(II) atoms present threefold Ga coordination, while O(III) shows fourfold [11]. These differences in atomic coordination between α-Ga_2O_3 and β-Ga_2O_3 lead to variations in physical, chemical, and gas sensing properties. For instance, the monoclinic β-Ga_2O_3 structure presents low symmetry and anisotropic charge transport properties, which are highly desired in gas sensing applications [10]. However, recent studies suggest that other phases, such as α-Ga_2O_3 and ε(κ)-Ga_2O_3, show excellent gas sensing capabilities as well [18–21]. Almaev et al. deposited epitaxial ε(κ)-Ga_2O_3 films on high-quality α-Ga_2O_3:Sn substrates using halide vapor-phase epitaxy (HVPE) and studied their responses to various gases [19]. The films showed the highest sensitivity to H_2 gas at 500 °C. In similar studies, Si^+-implanted α-Ga_2O_3 and Pt-contacted α-Ga_2O_3:Sn films demonstrated high responses to H_2 gas [20,21]. In the former, the variation of the Si^+ dose tuned the selectivity of the material toward CO and NH_3 gases, while in the latter, controlling Sn dopant concentration modulated the response of α-Ga_2O_3:Sn films to H_2. Moreover, mixed phases of Ga_2O_3 have received growing interest in gas sensing applications. Almaev et al. observed that HVPE-grown Pt-contacted polymorphic α/ε-Ga_2O_3 structures recorded a higher response to H_2 compared to α-Ga_2O_3 films. They attributed enhanced sensitivity to the reduction of the Schottky barrier height at the α/ε-Ga_2O_3 interface [22].

While significant progress has been made in understanding the material properties and gas sensing capabilities of various Ga_2O_3 phases, considerable research is still needed, particularly regarding their synthesis and structural optimization. The performance of Ga_2O_3-based sensors is significantly influenced by factors such as material phase, morphology, and synthesis method. Several synthesis methods have been adopted to prepare Ga_2O_3 structures, including epitaxial sputtering, chemical vapor deposition, and hydrothermal processing [11]. Among these, the hydrothermal method stands out due to its cost-effectiveness, simplicity, and the ability to precisely control important parameters such as growth temperature, time, and pH of the solution. These tunable parameters allow precise control of the material's morphology, which is important for optimizing gas sensing performance [23]. For example, hydrothermally synthesized Ga_2O_3 nanostructures, such as nanorods and nanowires, demonstrate a large surface area-to-volume ratio, significantly improving transport properties and enhancing gas sensing capabilities [23].

Previous studies suggest that the gas sensing properties of the α/β-Ga_2O_3 phase remain unexplored. Therefore, it is important to study these properties in α/β-Ga_2O_3 and compare them to those of other Ga_2O_3 polymorphs. In addition, due to limited reports on the gas sensing properties of the α-Ga_2O_3 phase, further studies are required to add to this pool of knowledge. This study focuses on a detailed investigation of the gas sensing properties of sensors based on α-Ga_2O_3, α/β-Ga_2O_3, and β-Ga_2O_3 phases, composed of mixed nanorods and nanowires. The samples were synthesized using the hydrothermal method and calcined at temperatures ranging from 550 °C to 950 °C. A comprehensive analysis was carried out to investigate the correlation between the microstructure, morphology, chemical state, textural properties, defect structure, and gas sensing properties, with a focus on how calcination temperature influences the gas sensing properties of Ga_2O_3 polymorphs.

2. Experimental section

2.1. Materials

Gallium nitrate hydrate ($Ga(NO_3)_3{\cdot}xH_2O$, 99.9 % purity) and ammonium hydroxide (NH_4OH, 28 %) were purchased from Sigma-Aldrich. All reagents were used without further purification.

2.2. Preparation of Ga_2O_3 powders

Ga_2O_3 powder samples were prepared using the hydrothermal method, as shown schematically in Fig. 1(a). A mass of 0.2557 (± 0.0001) g of $Ga(NO_3)_3{\cdot}xH_2O$ was dissolved in 10 mL of deionized (DI) water with vigorous stirring at 60 °C, resulting in a 0.1 M Ga^{3+} solution. NH_4OH was added dropwise using a micropipette at 5 s intervals until the pH reached 12. The resulting cloudy mixture was maintained at 60 °C for 1 hour, then microwaved for 1 hour at 150 °C and 100 W using a Discover 2.0 microwave synthesizer. The precipitate was washed multiple times with water and ethanol using centrifugation, then dried in an oven at 60 °C before being divided into smaller portions. Each portion was calcined separately in air at 550, 650, 750, 850, or 950 °C in a muffle furnace for 2 h, with a heating rate of 5 °C/min. The calcined samples were labeled S550, S650, S750, S850, or S950, based on their respective calcination temperature.

2.3. Sample characterization

The crystallinity and phase purity of the Ga_2O_3 powders were measured by X-ray diffraction using a Bruker D2 Phaser X-ray diffractometer equipped with a CuKα1 radiation source ($\lambda = 0.15406$ nm). The diffraction patterns were collected over a 2θ range from 15 ° to 70 ° with a step size of 0.02 ° The morphology of the powders was studied using scanning electron microscopy with a JEOL JSM-7500F field-emission scanning electron microscope operated at an accelerating voltage of 8 keV. To minimize surface charging, the samples were coated with carbon and gold-palladium before measurement. The microstructure of all samples was studied using transmission electron microscopy (TEM) with a JEOL TEM-2100 system operated at an accelerating voltage of 200 kV. The surface area and porosity of the samples were quantified using a Micromeritics TriStar 3000 surface-area analyzer. Prior to measurement, the powder samples were degassed at 200 °C for 2 h and subsequently cooled in a bath of liquid nitrogen. The chemical composition and electronic states of the samples were measured using a PHI 5000 Scanning ESCA Microprobe X-ray photoelectron spectrometer, equipped with a 100 μm diameter monochromatic Al-Kα beam ($h\nu = 1486.6$ eV). For XPS measurements, the Ga_2O_3 powder samples were pressed onto a 3 × 3 mm piece of conductive carbon tape to ensure good adhesion and electrical conductivity. The tape was then mounted onto the sample holder and placed into the XPS chamber for measurement. Surface charging was minimized using a low-energy Ar^+ gun and a low-energy neutralizer gun. Photoluminescence (PL) was used to study the defect

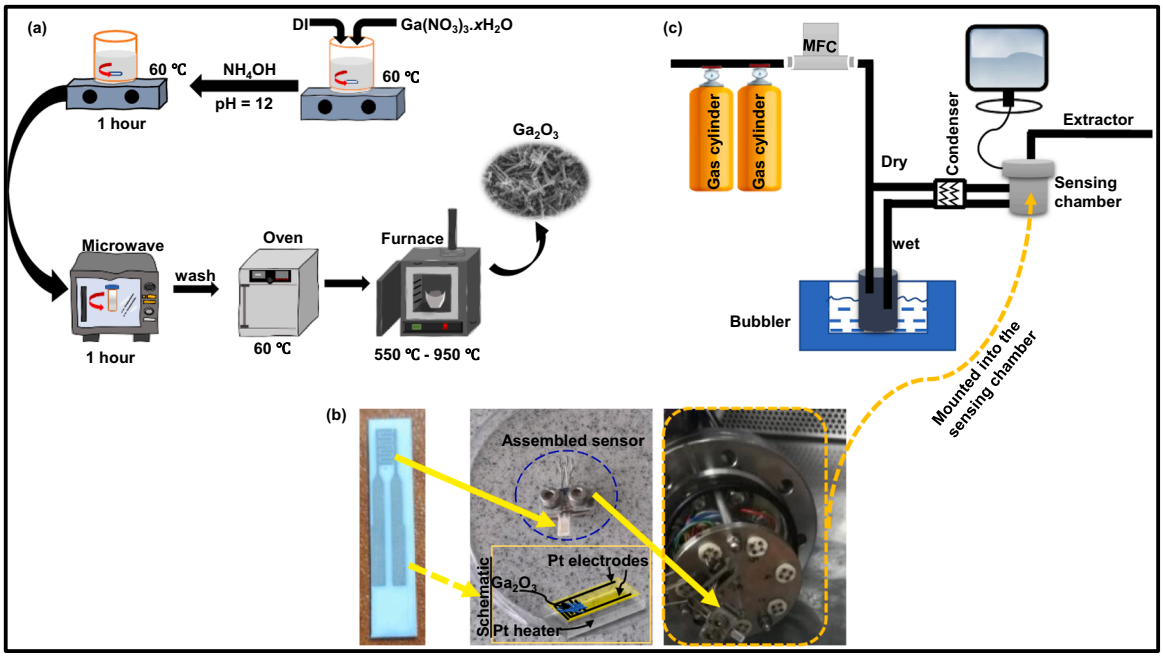

Fig. 1. (a) Schematic representation of the synthesis of Ga_2O_3 using the microwave-assisted hydrothermal method followed by calcination at different temperatures. (b) Fabrication process of Ga_2O_3-based sensing layer films on alumina substrates with platinum electrodes. (c) Experimental setup of the gas sensing system, including the test chamber, gas flow system, and measurement components.

properties of the samples. Spectra were measured using a Horiba QuantaMaster QM8000 spectrofluorometer with a Xenon lamp as the excitation source. The optimal excitation wavelength of 265 nm was used, and emission-corrected spectra were recorded in the range of 300 nm to 800 nm with a step size of 1 nm and an integration time of 0.1 s. A 295 nm optical high-pass filter was used to attenuate the signal from the excitation wavelength.

2.4. Ga_2O_3-based gas sensor preparation and testing

To prepare each Ga_2O_3 sensor layer, 10 mg of the sample was mixed with 0.05 mL of ethanol to form a slurry. The solution was deposited onto a purchased alumina substrate with Pt interdigitated electrodes and a Pt heater at the back (Fig. 1(b)). Each alumina substrate measured 2 mm in length and 0.6 mm in width, with a 150 μm gap between the Pt electrodes. Alumina substrates are commonly used in gas sensors due to their high thermal conductivity, excellent insulating properties, and low thermal expansion coefficient [24]. The sensing layer was annealed at 300 °C in a muffle furnace overnight with a heating rate of 5 °C/min to improve the adhesion to the substrate. The alumina substrate, now containing the sensing layer, was assembled into a 4-pin sensor element (Fig. 1(b)) and then inserted into a sample holder within the sensing chamber (Fig. 1(c)).

Gas sensing properties were measured using a KSGAS6S gas-sensing station (KANOSISTEC, Italy), with the sensor exposed to both dry and humid conditions at operating temperatures ranging from room temperature to 180 °C. Humid conditions within the sensing chamber were achieved by evaporating water in a bubbler set at 50 °C. The target gases were introduced into the sensing chamber by varying the flow rate ratios of synthetic air and compressed target gases using a mass flow controller to achieve the desired concentrations (in parts per million, ppm). The compressed gases, commercially available in cylinders, had the following concentrations: CO – 2074 ppm, C_2H_4 – 114 ppm, CH_4 – 103 ppm, NH_3 – 95 ppm, NO_2 – 200 ppm, and SO_2 – 200 ppm.

A 2 V bias was applied across the sensor, and its electrical resistance in synthetic air (R_a) and in the target gas (R_g) was measured using a Keithley 6487 picoammeter/voltage source meter. The response of the sensor to the presence of reducing and oxidizing gases was calculated by $(R_a - R_g)/R_g$ and $(R_g - R_a)/R_a$, respectively. The response and recovery times were calculated as the time taken by the sensor to reach 90 % of the total change in resistance upon gas exposure and removal, respectively.

3. Results and discussion

3.1. Crystal structure

Fig. 2(a) shows the XRD patterns of the calcined Ga_2O_3 samples. The XRD pattern of the S550 sample corresponds to the rhombohedral α-Ga_2O_3 phase (JCPDS No 06–0503), while that of S650 shows a coexistence of the α-Ga_2O_3 and monoclinic β-Ga_2O_3 phases (JCPDS No 76–0573). This indicates that an increase in the calcination temperature from 550 °C to 650 °C promotes the formation of crystal domains with varying orientations associated with both α-Ga_2O_3 and β-Ga_2O_3. This phase transformation can be attributed to thermal effects that facilitate atomic rearrangement, resulting in a thermodynamically more stable configuration. The rhombohedral phase, characterized by three equal axes and high symmetry [25], undergoes a symmetry change upon calcination, favoring the monoclinic phase with lower symmetry [26]. The XRD patterns of the S750, S850, and S950 samples were indexed to β-Ga_2O_3, with variations in diffraction peak intensities suggesting changes in thermally induced growth orientations as the lattice stabilizes into a configuration with the lowest symmetry. The phase transformation from α-Ga_2O_3 to β-Ga_2O_3 at calcination temperatures in the range of 550–650 °C has been reported in the literature [17,27]. The average crystallite sizes of the samples were estimated using the Scherrer equation [28], based on the peak position and full width at half maximum (FWHM) of the most intense diffraction peaks. The crystallite sizes were 18.2, 20.2, 10.3, 16.9, and 17.4 nm for S550, S650, S750, S850, and S950, respectively. These results suggest that an increase in calcination temperature enhances crystallite boundary movement, promoting the coalescence of smaller crystallites within the same Ga_2O_3 phase.

To complement the XRD results, HRTEM images were used to

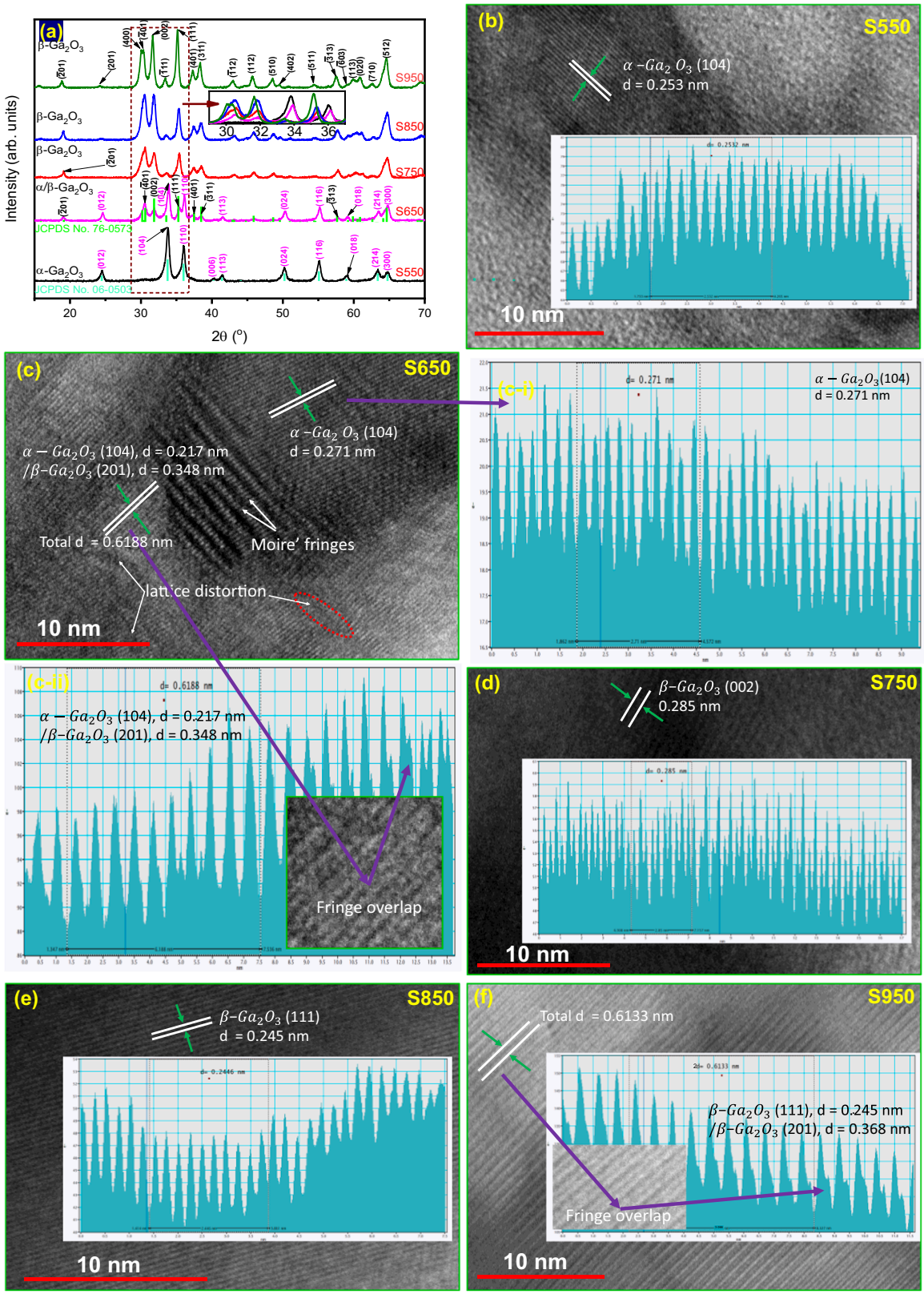

Fig. 2. (a) XRD patterns of Ga_2O_3 samples calcined at different temperatures. (b-f) HRTEM images and D-spacing histograms of α-Ga_2O_3, α/β-Ga_2O_3, and β-Ga_2O_3 samples. (c-i, c-ii) D-spacing histograms of α/β-Ga_2O_3.

provide additional microstructural insight. As shown in Fig. 2(b), the S550 sample presents the lattice fringes corresponding to the (104) crystallographic plane of the α-Ga_2O_3 phase, with an interplanar spacing (d-spacing) of 0.253 nm. In the S650 sample, mixed-phase features are observed. Fig. 2(c) and its corresponding histograms of the D-spacings in Figs. 2(c-i) and 2(c-ii) show lattice fringes associated with both α-Ga_2O_3 and β-Ga_2O_3 phases. Notably, the α-Ga_2O_3 (104) fringes presents a D-spacing of 0.271 nm. In addition, fringes with a combined spacing of

0.6188 nm were observed. This particular spacing does not match any known plane of the α-Ga_2O_3 phase. However, given the verified coexistence of α-Ga_2O_3 and β-Ga_2O_3 phases in this sample, as shown by XRD data in Fig. 2(a), and the appearance of Moiré patterns, the 0.6188 nm spacing can be attributed to the superposition of α-Ga_2O_3 (104) and β-Ga_2O_3 (201) planes, with individual D-spacings of 0.271 and 0.348 nm, respectively. The inset in Fig. 2(c-ii) further confirms this interpretation by showing overlapping fringes. This provides strong evidence of the coexistence and nanoscale intergrowth of the α- and β-Ga_2O_3 domains in the S650 sample, which is consistent with the XRD results. For samples S750 and S850 (Figs. 2(d) and 2(e)), HRTEM images show well-defined fringes corresponding to the (002) and (111) planes of β-Ga_2O_3, with D-spacings of 0.285 and 0.245 nm, respectively, indicating predominantly β-Ga_2O_3 phase composition. In the S950 sample (Fig. 2(f)), overlapping fringe patterns with a total D-spacing of 0.6133 are observed. Similar to the S650 sample, this overlap is attributed to the superposition of the β-Ga_2O_3 (111) and (201) planes, with D-spacings of 0.245 nm and 0.368 nm, respectively. These HRTEM results provide microstructural confirmation of the phase compositions and phase evaluation inferred from the XRD analysis.

3.2. Morphology and texture analysis

Gas sensing performance is strongly influenced by the material's surface properties, including morphology, specific surface area, porosity, and chemical composition [29]. The morphology of the synthesized Ga_2O_3 powders was studied using SEM, with the results shown in Fig. 3. The SEM images showed the coexistence of randomly oriented, non-uniform nanorods and nanowires. The S550 and S650 samples are dominated by nanorods, in contrast to the unannealed sample, as shown in the inset of Fig. 3(a). This suggests that the thermal energy supplied to the samples was sufficient to transform the GaOOH crystal structure of the unannealed sample into α-Ga_2O_3 and induce grain growth from nanowires to nanorods. However, the S750 sample shows more nanowires than nanorods, similar to the unannealed sample. This suggests that the supplied thermal energy induced the phase transformation from GaOOH to β-Ga_2O_3, limiting the amount of energy available for grain growth. Calcination at 850 °C and 950 °C provided sufficient energy to drive the transformation to β-Ga_2O_3 and promote the growth of the nanorods. The average diameters and lengths of the nanorods and nanowires for each sample were determined from the SEM images and were found to vary, as shown in Fig. 3(g).

A large specific surface area enhances the adsorption of oxygen molecules and target gases, which is important for gas sensing applications. To measure this property, BET measurements were performed. The results (Figs. 3(h-i)) show variations in surface area among the samples, influenced by differences in crystal structure (which determine the exposed surface areas) and morphology. The S750 sample (Fig. 3(c)) shows a relatively high specific surface area, which is attributed to the smaller diameters and lengths of the nanorods and nanowires observed in SEM analysis. Although the β-Ga_2O_3 phase remains stable beyond 750 °C, the S850 sample shows a significant decrease in surface area. This

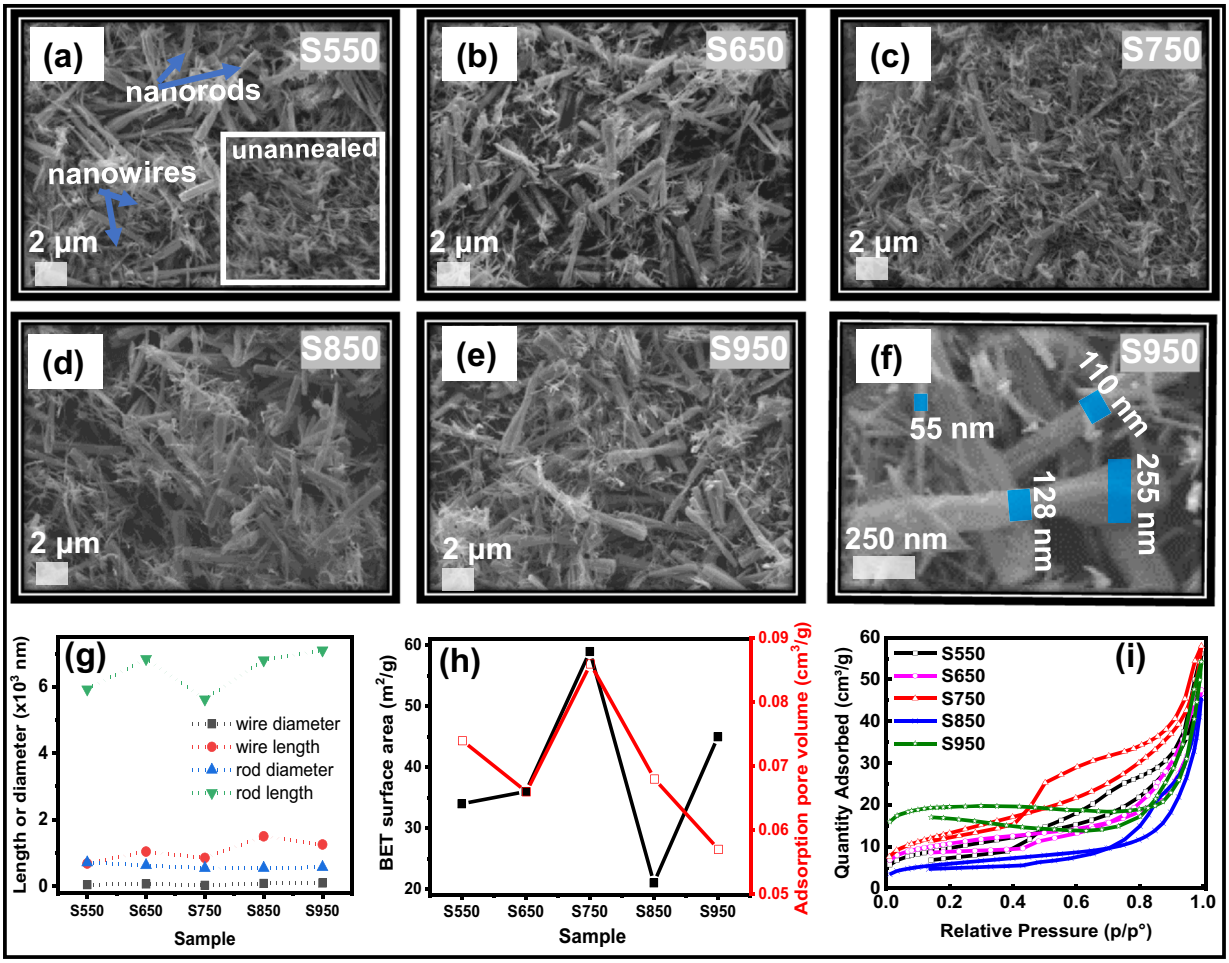

Fig. 3. (a–f) SEM images of Ga_2O_3 samples calcined at different temperatures. (g) Variation in nanorod/nanowire lengths and diameters across different calcination temperatures. (h) BET surface area and BJH pore volume data, presenting surface area and porosity trends. (i) N_2 adsorption-desorption isotherms of mesoporous Ga_2O_3 samples.

reduction is attributed to partial agglomeration and densification of the nanostructures (Fig. 3(d)), which reduces the accessible surface area despite the phase stability confirmed by XRD. Such morphological coalescence at intermediate temperatures could be linked with thermally driven particle growth and surface facets reorientation shown by varying XRD peaks in the β-Ga_2O_3 phase. Interestingly, a similar trend, though with a slightly higher surface area value in the S950 sample, was observed. It can be suggested that a more porous and less agglomerated morphology (Fig. 3(e)) leads to a recovery in the surface area. This non-monotonic behavior indicates that at higher temperatures, surface reconstruction and microstructural rearrangements promote the formation of new porosity or surface features that enhance surface accessibility. Therefore, the observed surface area variations are dependent more on the thermal-induced morphological dynamics than by phase changes alone. Further studies, including in situ high-temperature TEM or surface chemistry analysis, would be valuable to fully understand the mechanisms underlying these morphological transformations and their impact in surface area.

Porosity enhances gas molecule diffusion into the internal surfaces of the particles, improving sensor performance. Porosity was quantified using N_2 adsorption-desorption measurements. Fig. 3(i) shows Type-IV isotherms with Type-H3 hysteresis loops, which suggest that all the samples are mesoporous [30]. Fig. 3(h) shows the pore volume values, extracted using the Barrett-Joyner-Halenda (BJH) method. The S750 sample showed the highest pore volume among all samples, which is attributed to the minimal agglomeration of the nanowires and nanorods.

3.3. Surface chemistry of Ga_2O_3 samples

The adsorption of gas molecules on the sensing surface is influenced by the surface's chemical state and composition [7]. XPS was used to assess these properties in Ga_2O_3 samples, as shown in Fig. 4. The XPS survey scans in Fig. 4(a) confirm the presence of Ga and O species along with incidental Cr impurities. The adventitious carbon (C 1 s) signal originates from the carbon tape used for mounting the samples. For binding energy calibration, all high-resolution XPS spectra measured were referenced to the C 1 s peak at 284.8 eV. The high-resolution XPS spectra of the Ga 2p spectra presented in Fig. 4(b) show the Ga $2p_{3/2}$ and Ga $2p_{1/2}$ spin-orbit doublet with a separation of 26.8 eV, consistent with previous reports [31,32]. Peak fitting of the Ga $2p_{3/2}$ component with 100 % Gaussian curves showed two distinct sub-components: a higher binding energy peak attributed to Ga-O bonding (Ga^{3+} in Ga_2O_3), and a lower binding energy peak. The latter is assigned to non-stoichiometric Ga_2O_{3-x} species (labelled as Ga-O_x in Fig. 4(b)). The fitted Ga 2p positions remained essentially unchanged across the phase transition from α-Ga_2O_3 to β-Ga_2O_3. This is consistent with literature reports, as the intrinsic chemical shift between these polymorphs is typically small (≤ 0.2 eV) and often within the experimental resolution of the XPS measurements [31,33]. The ratio of the Ga-O_x peak area to the Ga-O peak area, calculated from the Ga $2p_{3/2}$ fits, decreased systematically with

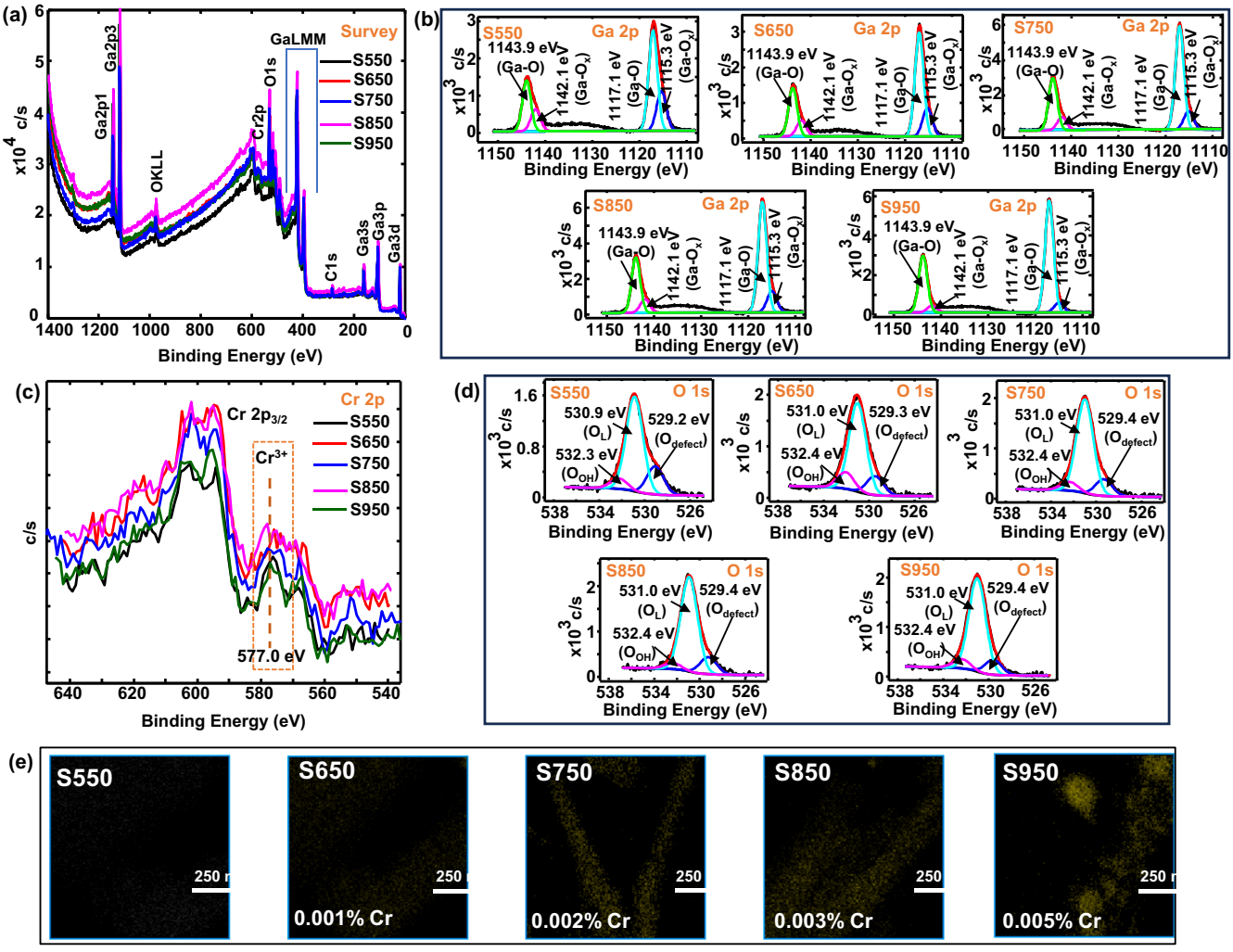

Fig. 4. (a) XPS survey spectra of Ga_2O_3 samples, identifying elemental composition. (b-d) High-resolution spectra of Ga 2p, O 1 s, and Cr 2p core levels. (e) STEM elemental mapping, illustrating the distribution of Cr^{3+} impurities at different calcination temperatures.

increasing calcination temperature and the phase transformation. Ratio values of 0.44, 0.31, 0.20, 0.22, and 0.10 were obtained for the S550, S650, S750, S850, and S950 samples, respectively. This trend reflects a reduction in oxygen-deficient gallium species as the β-phase stabilizes and the crystal structure becomes highly ordered. The decrease in non-stoichiometric Ga_2O_{3-x} content in β-Ga_2O_3 could be beneficial for gas sensing as it leads to a more stable and selective surface with fewer non-specific adsorption sites and higher lattice oxygen content which can promote specific gas-surface interactions.

The high-resolution XPS spectra of the O1s core level presented in Fig. 4(d) show broad and asymmetric spectra suggesting the presence of multiple oxygen species. The spectra were also fitted with 100 % Gaussian peaks and a Shirley background, after subtraction of background offset. Three components were identified in the α-Ga_2O_3 phase and these were: (i) the lattice oxygen (O_L) positioned at 531.0 eV, corresponding to the O^{2-} in the Ga_2O_3 lattice; (ii) a lower binding energy peak at 529.3 eV, attributed to defect-related oxygen species (O_{defect}); and a higher binding energy peak at 532.4 eV, assigned to adsorbed water or hydroxyl groups [31,32]. The small binding energy shifts (~ +0.1 eV) in the β-phase are consistent with changes in local bonding environments due to phase transformation. The area percentage of the defect-related oxygen peak decreased with the transition from α- to β-Ga_2O_3, indicating a reduction in the surface defects as the structure becomes more crystalline. The values were 20 %, 17 %, 15 %, 16 %, and 13 % for S550, S650, S750, S850, and S950, respectively. This effect is further shown by the increased lattice oxygen content because of increasing the calcination temperature. The area percentages of the O_L content were 71 %, 71 %, 79 %, 81 %, and 79 % for S550, S650, S750, S850, and S950, respectively. A relatively constant content of the lattice oxygen in the α/β-Ga_2O_3 phase can be explained by the competing effects of increased lattice stabilization which would increase lattice oxygen, and the initial structure disorder introduced during phase transformation which would decrease lattice oxygen. The amount of oxygen from adsorbed water/hydroxyl groups decreased with increasing calcination temperature, consistent with thermal desorption processes. The area percentages of -OH-related components were 9 %, 12 %, 6 %, 3 %, and 8 % for S550, S650, S750, S850, and S950, respectively. Notably, the α/β-Ga_2O_3 phase showed the highest content of adsorbed -OH, likely due to the higher density of surface defects and phase boundaries, which provide favorable sites for hydroxyl adsorption.

Fig. 4(c) shows the high-resolution XPS spectra for the Cr 2p core level, characterized by Cr $2p_{1/2}$ and Cr $2p_{3/2}$ spin-orbit doublets. The low intensity of the Cr signal suggests that the impurities are present at very low concentrations. The peak at 577.0 eV, corresponding to the Cr $2p_{3/2}$ component, suggests that Cr is present in the +3 oxidation state [34]. To further verify the presence of Cr^{3+} in Ga_2O_3 samples, elemental composition was studied using scanning transmission electron microscopy (STEM), as shown in Fig. 4(e). The STEM elemental mappings show that Cr^{3+} impurities are present at concentrations below 0.01 %, with an increasing trend as the calcination temperature rises. This temperature-dependent increase in Cr^{3+} concentration is likely due to enhanced Cr^{3+}out-diffusion toward the Ga_2O_3 surface [35]. These background Cr^{3+} impurities likely originate from the high purity (99.9 %) $Ga(NO_3)_3{\cdot}xH_2O$ precursor used in Ga_2O_3 synthesis, as previously reported [17,36].

Fig. 5(a) presents the room-temperature PL spectra for all α-Ga_2O_3, α/β-Ga_2O_3, and β-Ga_2O_3 samples. As indirect semiconductors, both α-Ga_2O_3 and β-Ga_2O_3 typically lack strong band-to-band emission due to the presence of self-trapped-holes (STH). Instead, the observed sub-gap emissions can be deconvoluted into primary emission bands namely, ultraviolet luminescence (UVL), blue luminescence (BL), green

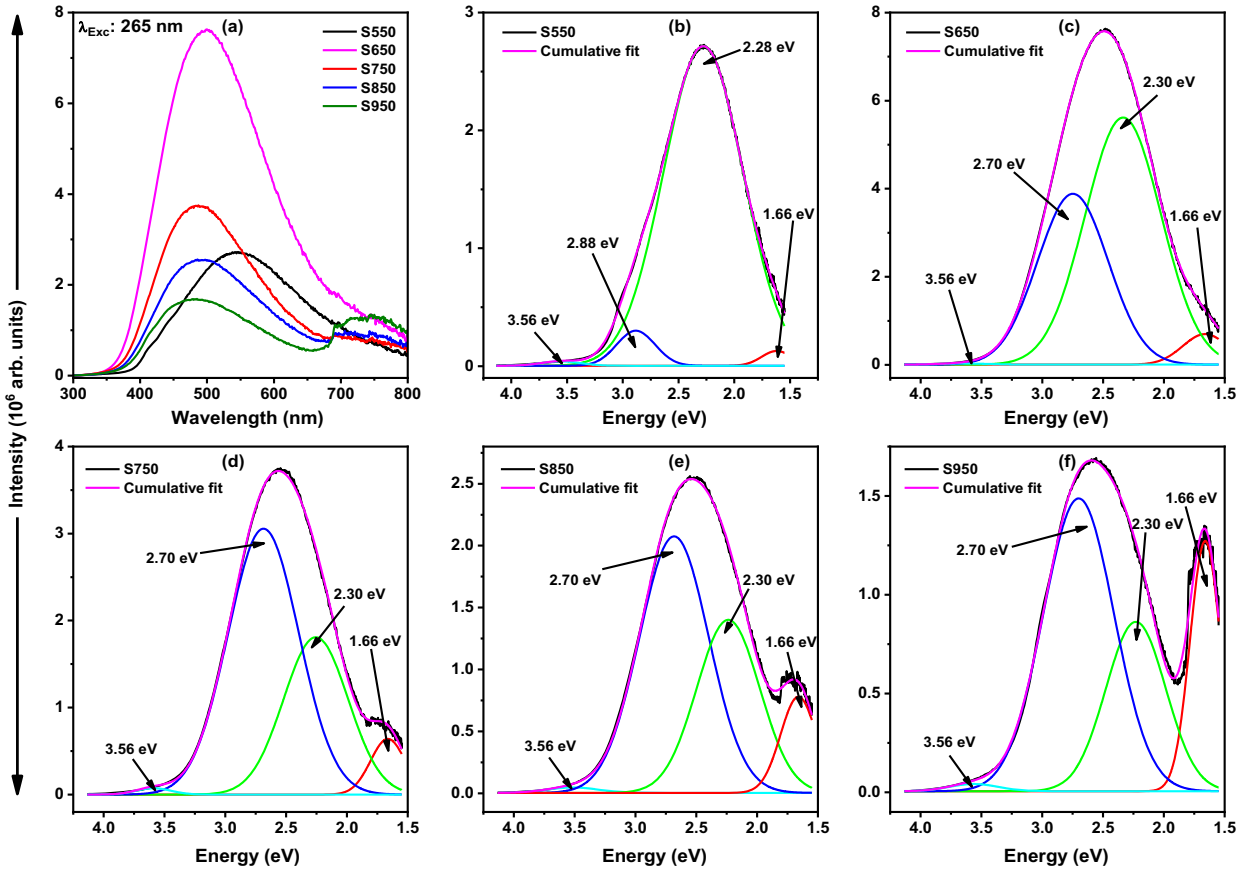

Fig. 5. (a) PL spectra of Ga_2O_3 samples at room temperature, showing defect-related emission. (b-f) Gaussian-fitted PL spectra, showing peak positions corresponding to defect states and Cr^{3+} impurity contributions.

luminescence (GL), and red luminescence (RL). These emission bands are associated with a variety of intrinsic and extrinsic defects, including self-trapped-electrons, oxygen vacancies (V_O), gallium vacancies (V_{Ga}), oxygen vacancy-gallium vacancy pairs (V_O-V_{Ga}), oxygen interstitials (O_i) and impurities such as interstitial nitrogen (N) and chromium (Cr^{3+}) [35,37,38].

The PL spectra in Figs. 5(d-f), deconvoluted using 100 % Gaussian curves with baseline correction without subtraction, show that the β-Ga_2O_3 samples present UVL, BL, and GL bands centered at 3.56, 2.70, and 2.30 eV, respectively. According to literature, the UVL band originates from radiative recombination of free electrons and STHs, with STHs in β-Ga_2O_3 located at approximately 1.1 eV above the valence band maximum (VBM) [38]. The BL band is attributed to donor-acceptor-pair (DAP) transitions involving deep donor oxygen vacancies and acceptors such as V_O-V_{Ga} pairs and V_{Ga}. Specifically, V_O defect levels at the O_I, O_{II}, and O_{III} lattice sites are situated at approximately 1.38, 1.76, and 1.56 eV below the conduction band minimum, respectively, while the V_O-V_{Ga} pair is located about 0.27 eV above VBM [38]. The V_{Ga} level is reported at approximately 0.66 eV above VBM [39]. Therefore, the BL in β-Ga_2O_3 nanorod/nanowires is primarily due to DAP transitions from V_{OII} to V_O-V_{Ga} while the GL is assigned to transitions from V_{OII} to V_{Ga}. The emission features in α-Ga_2O_3 are similar (Fig. 5(b)), so the same defect assignments are made for the S550 sample [37]. Minor in peak positions between phases can be attributed to differences in bandgap energies, which influence the energetic locations of defect levels [15,37]. The α/β-Ga_2O_3 intermediate phase showed similar transitions (Fig. 5(c)). A red luminescence (RL) band is observed in all samples at 1.66 eV, which is attributed to electron transitions from the $^4T_2$ and ^2E states to the $^4A_2$ ground state of Cr^{3+}impurities [36]. The splitting of these energy levels is strongly influenced by the crystal field of the Ga_2O_3 lattice [40]. As shown in Figs. 5(b-f), the intensity of Cr^{3+}-related RL band increases with higher calcination temperatures, likely due to the enhanced diffusion of Cr^{3+} impurities toward the Ga_2O_3 surface, as shown by STEM results (Fig. 4(e)).

Comparing the PL spectra across the series, the GL band decreases with increasing calcination temperature, while the BL band increases. This trend suggests that higher calcination temperatures favor the formation of oxygen vacancies (V_{OII}), leading to an increased density of the donor defects and acceptors in proximity. The highest PL intensity observed for S650 correlates with a high concentration of such radiative defects.

The evolution of the PL bands directly mirrors the trends observed in the XPS results. Specifically, the GL band in the PL spectra, which is associated with isolated oxygen vacancies, correlates with the O_{defect} identifies in the O 1 s XPS spectra. As the calcination temperature increases and the material transition from α-Ga_2O_3 to β-Ga_2O_3, both the GL intensity and the O_{defect} peak area decrease, indicating a reduction in isolated oxygen vacancy defects. Conversely, the BL band, attributed to DAP transitions involving V_O-V_{Ga} complexes, increases in intensity for the β-Ga_2O_3 samples, consistent with XPS evidence of evolving defect chemistry and a higher degree of crystallinity. Meanwhile, the enhanced RL band in the PL spectra supports the surface diffusion of Cr^{3+} impurities at higher calcination temperatures, as shown by STEM analysis.

Although the S650 (α/β-Ga_2O_3) sample shows a high density of oxygen vacancy sites favorable for gas adsorption, other factors such as lower surface area, lower crystallinity, higher adsorbed -OH content, and lower Cr content may limit its overall gas sensing performance. In contrast, the β-Ga_2O_3 samples, which display higher crystallinity, increased V_O-V_{Ga} defect concentration, higher surface area, and greater Cr content, are expected to offer improved gas sensing capabilities due to the combined effects of these structural and chemical features. A more detailed discussion of the gas sensing mechanism, including the roles of specific defect types and surface characteristics, is provided in the sensing mechanism section.

3.4. Gas sensing characteristics of Ga_2O_3-based gas sensors

Fig. 6(a) presents the electrical resistances in air (R_a) and 90 ppm CO (R_g) as a function of operating temperature (100–180 °C) for all Ga_2O_3-based sensors. The sensors showed typical semiconducting behavior, with resistance decreasing as temperature increased due to enhanced carrier excitation. The lower resistance allows adsorbed oxygen species to extract electrons from the conduction band at different operating temperatures, leading to resistance modulation [41]. The relationship between resistance and temperature was further studied using an Arrhenius plot (Fig. 6(b)) [42], from which activation energy values of 2.14, 2.50, 2.00, 2.00, and 1.83 were extrapolated for the S550, S650, S750, S850, and S950 sensors, respectively. These results suggest that the β-Ga_2O_3-based sensors may present superior gas sensing performance compared to those incorporating other phases.

The gas sensing performance of SMO-based sensors depends on operating temperature, with the highest response recorded at the optimal operating temperature, where oxygen species react most efficiently with the target gas [7]. To determine this temperature, the response to 90 ppm CO was measured over a temperature range of 25–180 °C. As shown in Fig. 6(c), all Ga_2O_3-based sensors achieved their highest response at 165 °C. Data below 100 °C were excluded due to a low signal-to-noise ratio. The lower responses observed below 165 °C suggest slow reaction kinetics at lower temperatures, while the decrease in response above 180 °C may result from excessive kinetic energy reducing oxide-gas interaction [6]. These temperature-dependent effects were less pronounced in the S550, S650, and S850 sensors, possibly due to weaker interactions between the sensing layers and CO molecules. Based on these results (Fig. 6(c)), all subsequent gas sensing measurements were carried out at 165 °C.

To measure the sensing capabilities of the Ga_2O_3-based sensors over a broad detection range, transient resistance curves were recorded for CO concentrations ranging from 10 ppm to 90 at 165 °C, as shown in Fig. 7(a). Consistent with the behavior of n-type Ga_2O_3-based gas sensors, the resistance decreased rapidly upon exposure to each CO concentration, reaching saturation during CO adsorption before returning to baseline resistance once the gas flow stopped. The magnitude of the resistance change increased with CO concentration across all sensors. Notably, β-Ga_2O_3-based sensors showed a greater resistance change at all concentrations, likely due to their conductive monoclinic crystal structure, which features highly anisotropic and polar surfaces that enhance gas interactions [43]. Among these, the sensor based on β-Ga_2O_3 calcined at 750 °C (S750) showed the highest resistance change, attributed to its large surface area and high porosity.

To determine the sensitivity and limit of detection (LoD) of the Ga_2O_3-based sensors, calibration curves were fitted to the concentration-response data for CO concentrations ranging from 10 ppm to 90 ppm, as shown in Fig. 7(b). Sensitivity, defined as the sensor response per analyte gas concentration, was obtained from the slopes of the calibration curves, yielding values of 0.91, 0.73, 1.30, 0.99, and 1.06 ppm^{-1} for the S550, S650, S750, S850, and S950 sensors, respectively. Furthermore, the LoD was extrapolated as the minimum concentration that could be measured with a 3:1 signal-to-noise ratio [44]. The LoD values for the S550, S650, S750, S850, and S950 sensors were 3.6, 5.1, 2.3, 4.5, and 2.3 ppm, respectively. Notably, the S750 sensor shows the highest sensitivity and lowest CO detection limit among all samples, likely due to combinatorial effects of a large surface area, low activation energy, and the presence of Cr^{3+} ions on the surface. Reported studies suggest that Cr^{3+} in β-Ga_2O_3 enhances surface reactivity [45].

Selectivity is an important parameter in classifying gas sensor performance. To measure selectivity, Ga_2O_3-based sensors were exposed to 90 ppm of various gases, including CH_4, C_2H_4, NH_3, NO_2, and SO_2 gases. Fig. 8(a) shows the response of all sensors to these gases at an operating temperature of 165 °C. The β-Ga_2O_3-based sensors (S750, S850, S950) showed the highest responses to CO compared to the other gases tested. Although cross-sensitivity to the other gases was observed, the

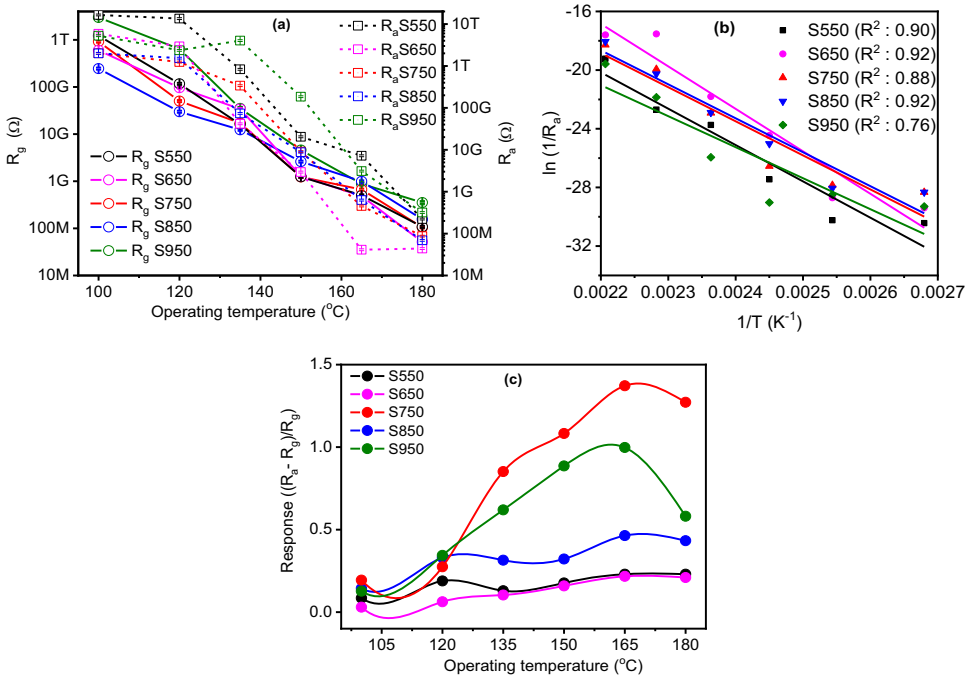

Fig. 6. (a) Variation of sensor resistance in air (R_a) and 90 ppm CO (R_g) with operating temperature (100–180 °C). (b) Arrhenius plots of ln(1/R_a) vs. 1/T demonstrating the effect of calcination temperature on sensor activation energies. (c) Sensor response to 90 ppm CO at various operating temperatures, showing optimal performance conditions for Ga_2O_3-based sensors.

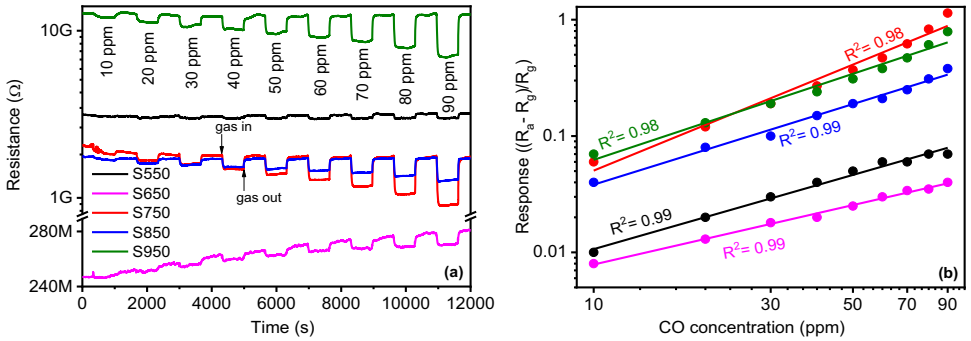

Fig. 7. (a) Transient resistance curves of Ga_2O_3-based sensors exposed to different CO concentrations (10–90 ppm) at 165 °C. (b) Calibration curves for CO detection, showing sensor sensitivity and linear response range.

distinctive response characteristics of the S750 sensor address this issue. The S750 sensor demonstrated selectivity coefficient ($K = R_{CO}/R_x$) of 11.8, 5.1, 6.2, 5.4, and 16.9 toward SO_2, NO_2, CH_4, NH_3, and C_2H_4, respectively, where R_{CO} represents the sensor response to CO and R_x denotes the response to the other gases [46]. These values, all greater than 1, demonstrate that interference from other gases has a minimal effect on CO detection, suggesting that the S750 sensor is capable of selective CO detection. In contrast, the α-Ga_2O_3 and α/β-Ga_2O_3 phases show enhanced responses to SO_2 and NH_3 gases, respectively. Further optimization of the sensor operating temperature for SO_2 and NH_3 detection was performed, as shown in Fig. 8(b). Both sensors show improved response at an elevated temperature of 180 °C, which was subsequently adopted for further characterization. These selectivity results highlight the varying affinities of different gases for the α-Ga_2O_3, α/β-Ga_2O_3, and β-Ga_2O_3 surfaces, suggesting that controlling polymorphism in Ga_2O_3 may offer a strategy for optimizing sensor selectivity for specific target gases.

For a gas sensor to be practically viable, it must not only provide consistent measurements under identical conditions but also maintain its performance over multiple cycles. To measure the reusability of the sensing materials, the S550, S650, S750, S850, and S950 sensors were exposed to 90 ppm of SO_2, CO, and NH_3 at their respective optimal operating temperatures. Fig. 8(c) presents the transient response-recovery curves, which show seven continuous and fully reversible sensing cycles for each sensor. The absence of significant deterioration in response magnitude, response time, or recovery time after multiple cycles demonstrates that the sensing materials can be reused without a decline in performance. The long-term stability of all Ga_2O_3 sensors was studied, as shown in Fig. 8(d). The S750, S850, and S950 sensors showed minor deviations (<4 %) from their initial response values over a 30-day period, demonstrating the high stability of the β-Ga_2O_3-based sensors. In contrast, the S550 sensor stabilized on day 10 after an initial 9 % decrease in response. However, the S650 sensor showed significant response fluctuations over time, suggesting instability. This instability may be attributed to prolonged exposure to various gases and humidity, as well as the inherent properties of the co-polymorph. The α/β-Ga_2O_3 co-polymorph presents relatively high surface activity [47], rendering it susceptible to irreversible reactions with undesirable active elements, which compromise long-term stability. These effects led to a 23 % decrease in response; however, overall, the sensor maintained

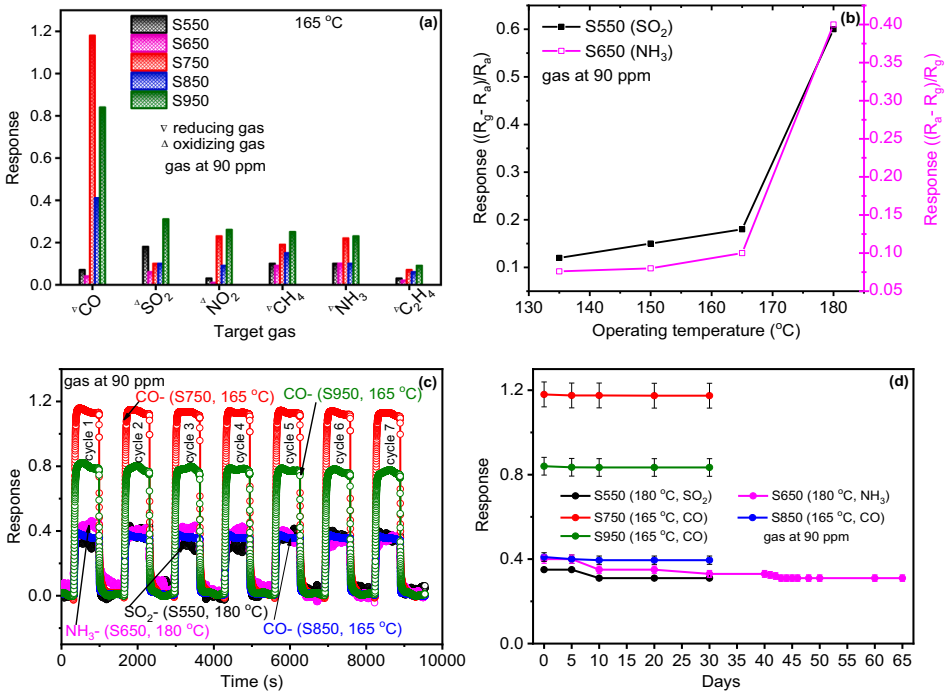

Fig. 8. (a) Selectivity of Ga_2O_3 sensors to 90 ppm of CO, NH_3, SO_2, NO_2, CH_4, and C_2H_4 gases at 90 ppm concentration. (b) Sensor response comparison of the S550 and S650 sensors exposed to 90 ppm of SO_2 and NH_3 gases, respectively, at operating temperatures of 135, 150, 165, and 180 °C. (c) Reproducibility curves of Ga_2O_3-based sensors over multiple gas exposure cycles. (d) Long-term sensor stability performance of the sensors.

acceptable stability after 43 days. The consistent response over multiple cycles (Fig. 8(c)) and the long-term stability (Fig. 8(d)) confirm that the Ga_2O_3-based sensors retain their gas sensing functionality over time. These results suggest that the sensors show good durability and reusability, making them suitable for practical applications.

The response and recovery times were calculated to determine the real-time monitoring capability of the S550, S650, S750, S850, and S950 sensors for SO_2, NH_3, and CO gases. The dynamic transient response curves toward 90 ppm of these gases, shown in Fig. 9(a), demonstrate sub-minute response times for the α-Ga_2O_3, α/β-Ga_2O_3, and β-Ga_2O_3 sensing layers. These rapid detection times are important for the immediate identification of toxic SO_2, NH_3, and CO gases. In addition, the extrapolated response times for the S750, S850, and S950 sensors show that tuning Ga_2O_3 properties by controlling the calcination temperature

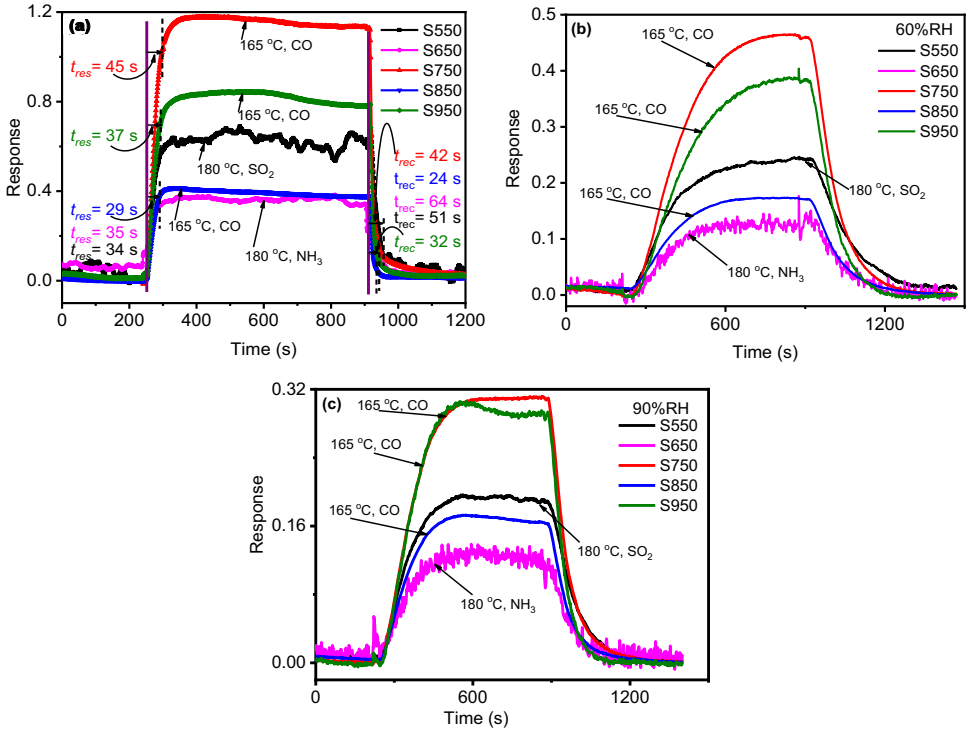

Fig. 9. Response of Ga_2O_3-based sensors measured under (a) dry (0 % RH), (b) 60 % RH, and (c) 90 % RH.

influences the sensor response times. The recovery times of the β-Ga_2O_3-based sensors were similar to their recovery times, whereas the recovery times of the α-Ga_2O_3 and α/β-Ga_2O_3-based sensors exceeded their respective adsorption times. This observation suggests that the desorption of SO_2 and NH_3 gases proceeded more slowly than their adsorption on these sensor surfaces.

Relative humidity (RH) influences gas adsorption kinetics and the sensitivity of the sensing material, posing challenges for developing highly sensitive gas sensors for real-world applications. Figs. 9(a-c) show the effects of RH on the response magnitude, response time, and recovery times of Ga_2O_3-based sensors exposed to 90 ppm of their target gases, measured at their optimal operating temperatures. The sensor response decreased, while the response times and recovery times increased with the introduction of 60 % RH and 90 % RH. These effects may be attributed to the competitive adsorption of water molecules on the surface, forming a monolayer of -OH groups that occupy active sites.

The gas detection performance of the α-Ga_2O_3, α/β-Ga_2O_3, and β-Ga_2O_3 sensors was further compared to other metal oxide-based sensors reported in the literature for SO_2, NH_3, and CO detection. As shown in Table 1, the β-Ga_2O_3 sensors demonstrate fast response and recovery times, high response, and low detection limits at relatively low operating temperatures for approximately the same CO concentration, without the need for sensor sensitization or modification with noble metals or perovskites. This study demonstrates that controlling the calcination temperature of the β-Ga_2O_3 enables the tuning of specific sensor parameters: high response at 750 °C, fast response and recovery times at 850 °C, and a low detection limit at 950 °C. Although the responses of α-Ga_2O_3 and α/β-Ga_2O_3 are relatively lower than those of the cited materials (Table 1), both phases show sub-minute response and recovery times, making them promising candidates for SO_2 and NH_3 detection. Therefore, the proposed sensing mechanisms of the α-Ga_2O_3, α/β-Ga_2O_3, and β-Ga_2O_3 materials are discussed in Section 3.5.

3.5. Gas sensing mechanism of Ga_2O_3-based sensors

The gas sensing mechanism of Ga_2O_3-based chemiresistive sensors follows the surface adsorption model, which is commonly applied in semiconductor metal oxide sensors. These sensors operate through direct charge transfer between ionized oxygen species and target gas molecules interacting with the sensing material. In this study, this principle is used to explain the enhanced CO, NH_3, and SO_2 sensing properties of n-type Ga_2O_3 nanorods/nanowires.

In ambient air, oxygen molecules adsorb onto the surface of Ga_2O_3 nanorods/nanowires, where they capture conducting electrons from the material. This process transforms the adsorbed oxygen into O^- species at operating temperatures of 165 °C and 180 °C, as described by Eq. (1) [60]. Consequently, an electron depletion layer (EDL) forms near the surface, as illustrated in Fig. 10(a(i)) [61]. The overlap of EDLs among adjacent Ga_2O_3 nanorods/nanowires increases sensor resistance (R_a

$$O^-_{2(ads)} + e^- \rightarrow 2O^-_{(ads)} \quad (100 < T_{oper} < 300^{\circ}C) \tag{1}$$

When exposed to reducing gases such as CO and NH_3, the ionized oxygen species oxidize these gas molecules into CO_2, N_2, and H_2O, as described by Eqs. (2) and (3), releasing captured electrons back into the Ga_2O_3 nanorods/nanowires. This electron release reduces the thickness of the EDL and decreases the electrical resistance, as shown in Fig. 10(b).

$$2CO_{(gas)} + 2O^-_{(ads)} \rightarrow 2CO_{2gas} + 2e^- \tag{2}$$

$$2NH_{3(gas)} + 3O^-_{(ads)} \rightarrow N_{2(gas)} + 3H_2O_{(gas)} + 3e^- \tag{3}$$

Conversely, when exposed to the oxidizing gas SO_2, the gas molecules undergo oxidation, forming SO_3^- species, as described by Eq. (4). In this process, SO_2 molecules capture free electrons from both the Ga_2O_3 nanorods/nanowires and the ionized oxygen species, leading to an expansion of the EDL as shown in Fig. 10(c), and a consequent increase in electrical resistance.

$$SO_{2(gas)} + O^-_{(ads)} \rightarrow SO_3^-{}_{(ads)} \tag{4}$$

The varying gas sensing performance of Ga_2O_3-based sensors can be attributed to a combination of factors, including the morphological characteristics, porosity, specific surface area, and nature and concentration of structural defects and impurities. The one-dimensional (1D) structure of nanorods/nanowires facilitates the overlapping of the EDLs along the nanowires/nanorods axis, creating a continuous electron transfer channel that improves sensor response [62]. The mesoporous nature of these Ga_2O_3 nanorod/nanowires, promotes efficient gas diffusion throughout the sensing layers, maximizing interaction between gas molecules and active sites. A large surface area provides additional reactive sites for gas adsorption and desorption, thereby enhancing the overall performance of the sensor.

Defect chemistry, as revealed by XPS and PL analyses, vary in Ga_2O_3 depending with the calcination temperature. In terms of gas sensing, oxygen vacancies (V_O^{2+}) act as active sites for the adsorption and

Table 1
Comparison of CO, SO_2, and NH_3 gas sensors based on SMO sensing materials. Key: NRs- nanorods, NPs- nanoparticles, NWs- nanowires, NSs – nanosheets, PNS- porous nanosolids, NFs- nanofibers. Abbreviations: Conc.- concentration, T– operating temperature, t_{res}- response time, t_{rec}- recovery time, Res.- response, Ref.- reference, ± - percentage fraction of ambient air, $^+$LoD (limit of detection). Response calculation methods: * $(R_a - R_g)/R_g$, ** $((R_a - R_g)/R_g) \times 100$ %, § $(R_g - R_a)/R_a$, §§ $((R_g - R_a)/R_a) \times 100$ %, & R_a/R_g, $ $(R_a/R_g) \times 100$ %, ‡ $((I_a - I_g)/I_a) \times 100$ %, where I represents the current, † $(R_S - R_0)/R_S$, and $$ $(G_g - G_a)/G_a$), where G represents the electrical conductance.

Gas	Material	Conc. (ppm)	T (°C)	t_{res} (s)	t_{rec} (s)	Res.	Ref.
CO	β-Ga_2O_3 (Sn) NRs– 750	115	500	–	–	$^{$$}$1.02	[18]
	ε-Ga_2O_3	±1.5 %	500	–	–	**25 %	[19]
	β-Ga_2O_3 LSFO NRs	100	500	~200	~500	*~70	[48]
	β-Ga_2O_3 NWs	200	200	–	–	§3.95	[49]
	β-Ga_2O_3 NWs	100	100	440	300	**6.61 %	[50]
	Pt/β-Ga_2O_3 NWs	100	100	650	750	**111.65 %	[50]
	Au/β-Ga_2O_3 NWs	100	RT	21.14	21.34	**~4.8 %	[51]
	β-Ga_2O_3 (Sn) – 950	120	500	–	–	$^{$$}$1.3	[18]
	ZnO NRs	100	RT	–	150	‡81.1	[52]
	ZnO NSs	100	300	25	36	&11.2	[53]
	SnO_2 PNS	100	RT	144	882	&64.5	[54]
	TiO_2 thin films	100	200	120	60	†−0.1	[55]
	Pt:CeO_2 NFs	100	800	50	–	$1	[56]
	Pd:SnO_2 NFs	100	385	23.7	3.7	&11.3	[57]
	β-Ga_2O_3 NRs/NWs (S750)	90 ($^+$2.3)	165	45	42	*1.18	This study
	β-Ga_2O_3 NRs/NWs (S850)	90 ($^+$4.5)	165	29	24	*0.41	This study
	β-Ga_2O_3 NRs/NWs (S950)	90 ($^+$2.3)	165	37	32	*0.84	This study
SO_2	Pt-WO_3 NPs	8 ($^+$0.1)	160	150	200	&17.07	[58]
	Al-WO_3 NPs	8 ($^+$0.1)	290	10	20	&2.6	[58]
	α-Ga_2O_3 NRs/NWs	90	165	34	51	§0.6	This study
NH_3	β-Ga_2O_3 NRs	160	RT	–	–	§§~185 %	[14]
	β-Ga_2O_3 (Sn) NRs - 1000	115	500	–	–	$^{$$}$1.1	[16]
	β-Ga_2O_3 NWs	200	150			$~119 %	[59]
	α/β-Ga_2O_3 NRs/NWs (S650)	90	165	36	64	*0.4	This study

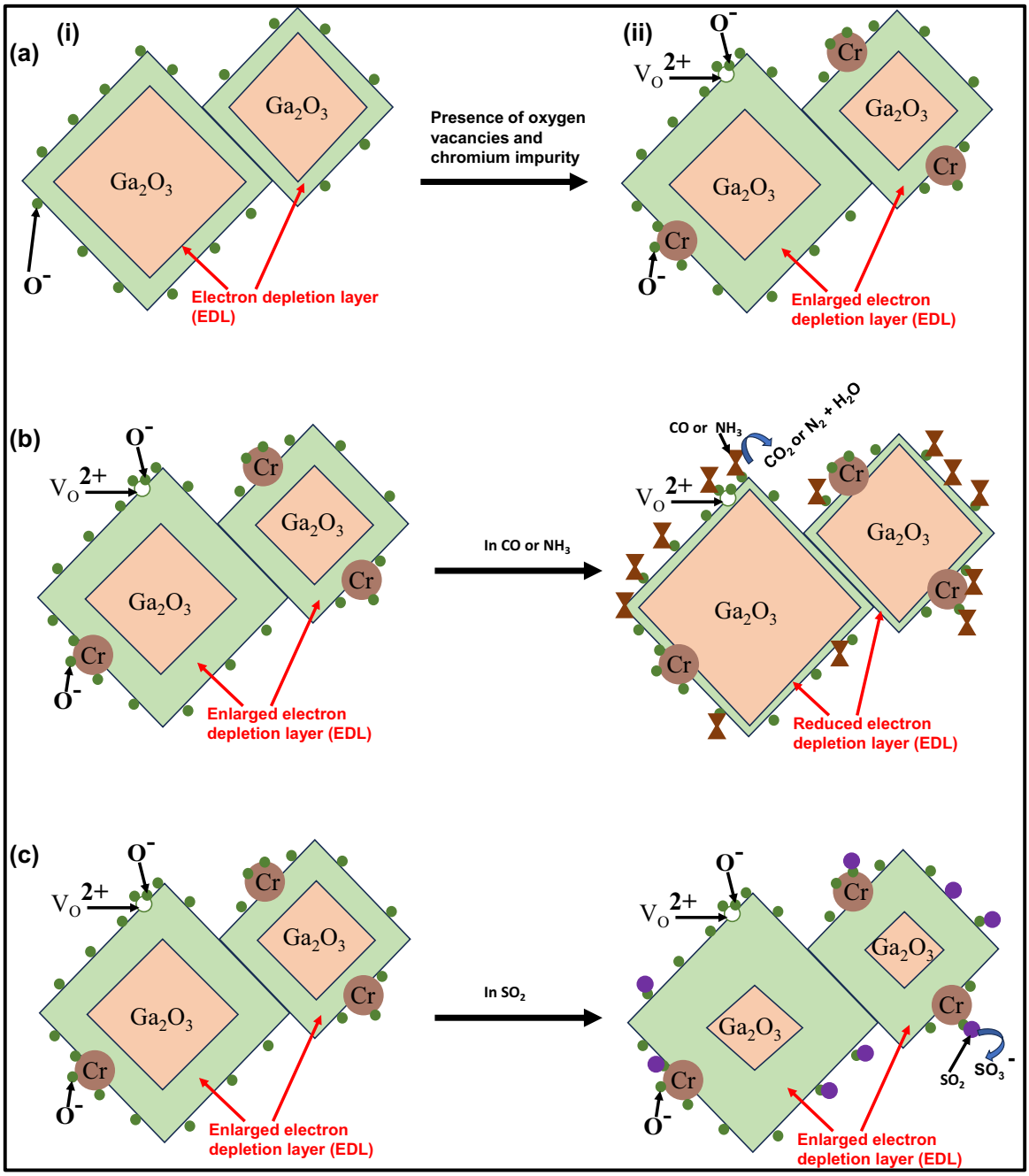

Fig. 10. Schematic diagram illustrating variations in the electron depletion layer of n-type Ga_2O_3 nanorods/nanowires under different gas exposure conditions: (a) in air, (b) CO and NH_3, and (c) SO_2.

ionization of oxygen species on the metal oxide sensor surface. An increased concentration of these vacancies leads to greater adsorption of oxygen species, which capture electrons from the sensing material, thereby expanding the EDL. This expansion increases the baseline resistance of the sensor, as shown in Fig. 10(a(ii)), and provides a larger pool of reactive oxygen species available to interact with the target gas. Consequently, the resistance modulation upon gas exposure is more pronounced, resulting in an enhanced sensing response [63]. Similarly, the presence of background Cr^{3+} impurities can modify the local electronic environment, facilitating charge transfer processes critical for sensing. They may also promote the adsorption of oxygen species, contributing to the enlargement of the EDL as shown in Fig. 10(a(ii)), and result in high sensitivity of the sensing material.

Therefore, the higher sensing performance observed from the β-Ga_2O_3 sensors (S750, S850, S950) can be attributed to the synergy of high crystallinity caused by high-temperature calcination, large surface area that is linked to small crystallite sizes and intrinsically small dimensions, improved transport properties due to more nanowires, low content of adsorbed -OH species on the surfaces, and high content of Cr^{3+} and V_O-V_{Ga} complex defects. In contrast, the low response recorded from the α/β-Ga_2O_3 phase (S650) can be due to high content of adsorbed -OH which reduces the active sites available for adsorption of oxygen species. While this sample showed the highest oxygen vacancies content which could have increased the density of adsorbed oxygen species, its relatively low surface area, lower crystallinity, and lower Cr^{3+} active sites may have additionally limited its overall sensing performance. In the case of the S550 sensor, the high content of non-stoichiometric gallium oxide, low Cr^{3+} on the surface, and presence of adsorbed -OH

may have limited the number of definitive sites available for oxygen adsorption and gas-surface interactions. However, it is important to note that this sensor showed an impressive low detection limit (concentration) and high sensitivity when applied in the detection of CO, though the response was low. These commendable attributes can be ascribed to the relatively high porosity shown by the sensor. The porosity of the sensor was the second highest in the series of all samples.

Overall, the outperformance by the S750 sensor is attributed to the morphology with more nanowires, high porosity, abundant V_O-V_{Ga} complexes, high crystallinity, increased Cr^{3+} impurities on the surface, and the significantly large surface area. Collectively, these results highlight that optimal gas sensing in Ga_2O_3 nanorods/nanowires arises not only from a high density of active defect sites, but also from the interplay of structural order, surface area, and the presence of catalytic impurities such as Cr^{3+}, which together govern the adsorption, charge transfer, and resistance modulation processes fundamental to chemiresistive sensing.

Further studies, particularly on simulated Ga_2O_3 surfaces containing Cr^{3+}, may provide valuable insights into the sensing mechanism of Ga_2O_3 with incidental impurities. In addition, investigating the effects of grain boundaries and oxygen defects in α/β-Ga_2O_3 could offer a better understanding of how phase mixing influences the sensing behavior of Ga_2O_3.

4. Conclusion

In this study, α-Ga_2O_3, α/β-Ga_2O_3, and β-Ga_2O_3 nanostructures were synthesized using a microwave-assisted hydrothermal method followed by calcination at different temperatures. SEM results showed nanorod/nanowire morphology, while BET results confirmed the mesoporous nature of the materials. XRD results confirmed the temperature dependence of Ga_2O_3 structural properties, while XPS, PL, and TEM investigations showed variations in defect concentrations due to calcination-induced phase transformations. Notably, incidental Cr^{3+} ions out-diffused from the bulk to the surface at higher calcination temperatures, altering the surface activity of Ga_2O_3 materials. Among the sensors, the β-Ga_2O_3 sensor (S750) showed the highest response (1.18) at a low operating temperature of 165 °C. The sensor showed excellent repeatability and stability, with a sensitivity of 1.30 ppm^{-1}, a detection limit of 2.3 ppm, and rapid response and recovery times of 45 s and 42 s, respectively, toward CO. The exceptional gas sensing performance is attributed to the sensor's large surface area, porous structure, and the presence of V_O-V_{Ga} complex defects and surface Cr^{3+} ions. However, the response decreased under high-humidity conditions due to the adsorption of water molecules. To mitigate this effect, the incorporation of a hydrophobic or sieve layer on the sensor is recommended for future studies. The α-Ga_2O_3 and α/β-Ga_2O_3 sensors showed the highest responses to SO_2 and NH_3, respectively, at an operating temperature of 180 °C, with response values of 0.6 and 0.4, respectively. Due to their rapid response times and recovery times, the β-Ga_2O_3 (S750), α-Ga_2O_3 (S550) and α/β-Ga_2O_3 (S650) sensors are promising candidates for detecting CO, SO_2, and NH_3 in indoor air quality monitoring. These observations show that controlling Ga_2O_3 polymorphism enables the optimization of gas sensing properties, particularly for CO, SO_2, and NH_3 detection.

CRediT authorship contribution statement

Nyepudzai C. Gatsi: Writing – original draft, Validation, Methodology, Investigation, Formal analysis, Data curation, Conceptualization. **Murendeni I. Nemufulwi:** Data curation. **Gugu H. Mhlongo:** Writing – review & editing, Supervision, Resources, Methodology, Investigation, Formal analysis, Data curation, Conceptualization. **Nosipho Moloto:** Supervision, Funding acquisition. **Rudolph M. Erasmus:** Supervision, Data curation. **Elizabeth Coetsee:** Formal analysis, Data curation. **Hendrik C. Swart:** Writing – review & editing, Formal analysis. **Odireleng M. Ntwaeaborwa:** Writing – review & editing, Supervision, Resources, Methodology, Investigation, Funding acquisition, Formal analysis, Conceptualization.

Declaration of competing interest

The authors declare that they have no known competing financial interests or personal relationships that could have appeared to influence the work reported in this paper.

Acknowledgements

This study was funded by the Organization for Women in Science for the Developing World (OWSD) and Sida (Swedish International Development Cooperation Agency), the National Research Foundation (NRF), South Africa, and the Council for Scientific and Industrial Research (CSIR), South Africa.

Data availability

Data will be made available on request.

References

[1] L. Al-Ghussain, Global warming: review on driving forces and mitigation, Environ. Prog. Sustain. Energy 38 (1) (2019) 13–21, https://doi.org/10.1002/ep.13041.
[2] World Health Organization, WHO Global Air Quality guidelines: Particulate Matter (PM2. 5 and PM10), Ozone, Nitrogen Dioxide, Sulfur Dioxide and Carbon Monoxide, World Health Organization, 2021.
[3] C.L. Townsend, R.L. Maynard, Effects on health of prolonged exposure to low concentrations of carbon monoxide, Occup. Environ. Med. 59 (10) (2002) 708–711, https://doi.org/10.1136/oem.59.10.708.
[4] I. Manisalidis, E. Stavropoulou, A. Stavropoulos, E. Bezirtzoglou, Environmental and health impacts of air pollution: a review, Front. Public Health 8 (2020) 505570, https://doi.org/10.3389/fpubh.2020.00014.
[5] M.S. Chavali, M.P. Nikolova, Metal oxide nanoparticles and their applications in nanotechnology, SN. Appl. Sci. 1 (2019) 607, https://doi.org/10.1007/s42452-019-0592-3.
[6] C. Wang, L. Yin, L. Zhang, D. Xiang, R. Gao, Metal oxide gas sensors: sensitivity and influencing factors, Sensors 10 (3) (2010) 2088–2106, https://doi.org/10.3390/s100302088.
[7] B. Saruhan, R.L. Fomekong, S. Nahirniak, Influences of semiconductor metal oxide properties on gas sensing characteristics, Front. Sens. (Lausanne) 2 (2021) 657931, https://doi.org/10.3389/fsens.2021.657931.
[8] M.A. Franco, P.P. Conti, R.S. Andre, D.S. Correa, A review on chemiresistive ZnO gas sensors, Sens. Actuators. Rep. 4 (2022) 100100, https://doi.org/10.1016/j.snr.2022.100100.
[9] Y. Masuda, Recent advances in SnO_2 nanostructure based gas sensors, Sens. Actuators B: Chem. 364 (2022) 131876, https://doi.org/10.1016/j.snb.2022.131876.
[10] H. Zhai, Z. Wu, Z. Fang, Recent progress of Ga_2O_3-based gas sensors, Ceram. Int. 48 (17) (2022) 24213–24233, https://doi.org/10.1016/j.ceramint.2022.06.066.
[11] F. Shi, H. Qiao, Preparations, properties and applications of gallium oxide nanomaterials–A review, Nano Sel. 3 (2) (2022) 348–373, https://doi.org/10.1002/nano.202100149.
[12] S.J. Pearton, J. Yang, P.H. Cary IV, F. Ren, J. Kim, M.J. Tadjer, M.A. Mastro, A review of Ga_2O_3 materials, processing, and devices, Appl. Phys. Rev. 5 (2018) 011301, https://doi.org/10.1063/1.5006941.
[13] J. Zhu, Z. Xu, S. Ha, D. Li, K. Zhang, H. Zhang, J. Feng, Gallium oxide for gas sensor applications: a comprehensive review, Materials. (Basel) 15 (2022) 7339, https://doi.org/10.3390/ma15207339.
[14] R. Pilliadugula, N. Krishnan, G, Effect of pH dependent morphology on room temperature NH_3 sensing performances of β-Ga_2O_3, Mater. Sci. Semicond. Process. 112 (2020) 105007, https://doi.org/10.1016/j.mssp.2020.105007.
[15] N.C. Gatsi, G.H. Mhlongo, N. Moloto, R.M. Erasmus, O.M. Ntwaeaborwa, Effects of reaction pH on regular nanorods and hierarchically structured β-Ga2O3 and their isopropanol sensing capabilities, Materialia (Oxf) 34 (2024) 102101, https://doi.org/10.1016/j.mtla.2024.102101.
[16] A. Sharma, M. Varshney, H. Saraswat, S. Chaudhary, J. Parkash, H.-J. Shin, K.-H. Chae, S.-O. Won, Nano-structured phases of gallium oxide (GaOOH, α-Ga_2O_3, β-Ga_2O_3, γ-Ga_2O_3, δ-Ga_2O_3, and ε-Ga_2O_3): fabrication, structural, and electronic structure investigations, Int. Nano Lett. 10 (1) (2020) 71–80, https://doi.org/10.1007/s40089-020-00295-w.
[17] N.C. Gatsi, G.H. Mhlongo, N. Moloto, R.M. Erasmus, P. Mashazi, T. Nyokong, O. M. Ntwaeaborwa, Hierarchically-ordered nanorods of Ga_2O_3 derived from microwave-assisted hydrothermal approach: investigation of calcination-induced structural evolution and optical behavior, Mater. Today Commun. 33 (2022) 104808, https://doi.org/10.1016/j.mtcomm.2022.104808.

[18] N. Vorobyeva, M. Rumyantseva, V. Platonov, D. Filatova, A. Chizhov, A. Marikutsa, I. Bozhev, A. Gaskov, Ga_2O_3(Sn) oxides for high-temperature gas sensors, Nanomaterials 11 (11) (2021) 2938, https://doi.org/10.3390/nano11112938.

[19] A. Almaev, V. Nikolaev, P. Butenko, S. Stepanov, A. Pechnikov, N. Yakovlev, I. Sinyugin, S. Shapenkov, M. Scheglov, Gas sensors based on pseudohexagonal phase of gallium oxide, Phys. Status Solidi (b) 259 (2) (2022) 2100306, https://doi.org/10.1002/pssb.202100306.

[20] N. Yakovlev, A. Almaev, P. Butenko, D. Tetelbaum, A. Mikhaylov, A. Nikolskaya, A. Pechnikov, S. Stepanov, B. Mikhail, À. Chikiryaka, V. Nikolaev, Effect of Si^+ ion implantation in α-Ga_2O_3 films on their gas sensitivity, IEEe Sens. J. 23 (3) (2022) 1885–1895, https://doi.org/10.1109/JSEN.2022.3229707.

[21] A.V. Almaev, V.I. Nikolaev, N.N. Yakovlev, P.N. Butenko, S.I. Stepanov, A. I. Pechnikov, M.P. Scheglov, E.V. Chernikov, Hydrogen sensors based on Pt/α-Ga_2O_3: sn/Pt structures, Sens. Actuators B: Chem. 364 (2022) 131904, https://doi.org/10.1016/j.snb.2022.131904.

[22] A.V. Almaev, V.I. Nikolaev, S.I. Stepanov, A.I. Pechnikov, A.V. Chikiryaka, N. N. Yakovlev, V.M. Kalygina, V.V. Kopyev, E.V. Chernikov, Hydrogen influence on electrical properties of Pt-contacted α-Ga_2O_3/ϵ-Ga_2O_3 structures grown on patterned sapphire substrates, J. Phys. D. Appl. Phys. 53 (41) (2020) 414004, https://doi.org/10.1088/1361-6463/ab9c69.

[23] J.-L. Chiang, B.K. Yadlapalli, M.-I. Chen, D.-S. Wuu, A review on gallium oxide materials from solution processes, Nanomaterials 12 (20) (2022) 3601, https://doi.org/10.3390/nano12203601.

[24] J. Kita, F. Schubert, F. Rettig, A. Engelbrecht, A. Groß, R. Moos, Ceramic alumina substrates for high-temperature gas sensors–Implications for applicability, Procedia Eng. 87 (2014) 1505–1508, https://doi.org/10.1016/j.proeng.2014.11.584.

[25] G. Yang, P.R. Romeo, A. Apostoluk, B. Vilquin, First principles study on the lattice thermal conductivity of α-phase Ga_2O_3, J. Vac. Sci. Technol. 40 (5) (2022), https://doi.org/10.1116/6.0001870.

[26] C. Kranert, C. Sturm, R. Schmidt-Grund, M. Grundmann, Sci. Rep. 6 (1) (2016) 35964, https://doi.org/10.1038/srep35964.

[27] X. Wang, Q. Xu, F. Fan, X. Wang, M. Li, Z. Feng, C. Li, Study of the phase transformation of single particles of Ga_2O_3 by UV-raman spectroscopy and high-resolution TEM, Chem. Asian J. 8 (9) (2013) 2189–2195, https://doi.org/10.1002/asia.201300433.

[28] A. Monshi, M.R. Foroughi, M.R. Monshi, Modified Scherrer equation to estimate more accurately nano-crystallite size using XRD, World J. Nano Sci. Eng. 2 (3) (2012) 154–160, https://doi.org/10.4236/wjnse.2012.23020.

[29] Edited by V.E. Bochenkov, G.B. Sergeev, Sensitivity, selectivity, and stability of gas-sensitive metal-oxide nanostructures, in: A. Umar, Y-B Hahn (Eds.), Metal Oxide Nanostructures and Their Applications, America Scientific Publishers, 2010, pp. 31–52. Edited by, https://api.semanticscholar.org/CorpusID:30372007.

[30] M. Thommes, K. Kaneko, A.V. Neimark, J.P. Olivier, F. Rodriguez-Reinoso, J. Rouquerol, K.S.W. Sing, Physisorption of gases, with special reference to the evaluation of surface area and pore size distribution (IUPAC Technical Report), Pure Appl. Chem. 87 (9–10) (2015) 1051–1069, https://doi.org/10.1515/pac-2014-1117.

[31] T.A. Chowdhury, XPS depth profile study of sprayed Ga_2O_3 thin films, Engineering 15 (8) (2023) 459–466, https://doi.org/10.4236/eng.2023.158035.

[32] A. Mahmoodinezhad, C. Janowitz, F. Naumann, P. Plate, H. Gargouri, K. Henkel, D. Schmeißer, J.I. Flege, Low-temperature growth of gallium oxide thin films by plasma-enhanced atomic layer deposition, J. Vac. Sci. Technol. 38 (2020) 022404, https://doi.org/10.1116/1.5134800.

[33] L. Qu, J. Ji, X. Liu, Z. Shao, M. Cui, Y. Zhang, Z. Fu, Y. Huang, G. Yang, W. Feng, Oxygen-vacancy-dependent high-performance α-Ga_2O_3 nanorods photoelectrochemical deep UV photodetectors, Nanotechnology. 34 (2023) 225203, https://doi.org/10.1088/1361-6528/acbfbd.

[34] W. Zhang, S. Song, M. Nath, Z. Xue, G. Ma, Y. Li, Inhibition of Cr^{6+} by the formation of in-situ Cr^{3+} containing solid-solution in Al_2O_3–CaO–Cr_2O_3–SiO_2 system, Ceram. Int. 47 (2021) 9578–9584, https://doi.org/10.1016/j.ceramint.2020.12.092.

[35] S. Wu, Z. Liu, H. Yang, Y. Wang, Effects of annealing on surface residual impurities and intrinsic defects of β-Ga_2O_3, Crystals. (Basel) 13 (7) (2023) 1045, https://doi.org/10.3390/cryst13071045.

[36] A. Luchechko, V. Vasyltsiv, L. Kostyk, O. Tsvetkova, B. Pavlyk, The effect of Cr^{3+} and Mg^{2+} impurities on thermoluminescence and deep traps in β-Ga_2O_3 crystals, ECS J. Sol. Stat. Sci. Technol. 9 (4) (2020) 045008, https://doi.org/10.1149/2162-8777/ab8b4d.

[37] Z. Wang, X. Chen, F.-F. Ren, S. Gu, J. Ye, Deep-level defects in gallium oxide, J. Phys. D. Appl. Phys. 54 (2021) 043002, https://doi.org/10.1088/1361-6463/abbeb1.

[38] X. Zhu, Y.-W. Zhang, S.-N. Zhang, X.-Q. Huo, X.-H. Zhang, Z.-Q. Li, Defect energy levels in monoclinic β-Ga_2O_3, J. Lumin. 246 (2022) 118801, https://doi.org/10.1016/j.jlumin.2022.118801.

[39] C.-H. Ho, C.-Y. Tseng, L.-C. Tien, Thermoreflectance characterization of β-Ga_2O_3 thin-film nanostrips, Opt. Express. 18 (2010) 16360–16369, https://doi.org/10.1364/OE.18.016360.

[40] G. Naresh-Kumar, H. MacIntyre, S. Subashchandran, P.R. Edwards, R.W. Martin, K. Daivasigamani, K. Sasaki, A. Kuramata, Origin of red emission in β-Ga_2O_3 analyzed by cathodoluminescence and photoluminescence spectroscopy, Phys. Status Solidi (b) 258 (2) (2021) 2000465, https://doi.org/10.1002/pssb.202000465.

[41] A. Heilig, N. Bârsan, U. Weimar, M. Schweizer-Berberich, J.W. Gardner, W. Göpel, Gas identification by modulating temperatures of SnO_2-based thick film sensors, Sens. Actuators B: Chem. 43 (1) (1997) 45–51, https://doi.org/10.1016/S0925-4005(97)00096-8.

[42] J. Crapse, N. Pappireddi, M. Gupta, S.Y. Shvartsman, E. Wieschaus, M. Wühr, Evaluating the Arrhenius equation for developmental processes, Mol. Syst. Biol. 17 (8) (2021) e9895, https://doi.org/10.15252/msb.20209895.

[43] Y. Zhang, A. Mauze, J.S. Speck, Anisotropic etching of β-Ga_2O_3 using hot phosphoric acid, Appl. Phys. Lett. 115 (1) (2019), https://doi.org/10.1063/1.5093188.

[44] J. Burgués, J.M. Jiménez-Soto, S. Marco, Estimation of the limit of detection in semiconductor gas sensors through linearized calibration models, Anal. Chim. Acta 1013 (2018) 13–25, https://doi.org/10.1016/j.aca.2018.01.062.

[45] A.V. Almaev, E.V. Chernikov, N.A. Davletkildeev, D.V. Sokolov, Oxygen sensors based on gallium oxide thin films with addition of chromium, Superlattices. Microstruct. 139 (2020) 106392, https://doi.org/10.1016/j.spmi.2020.106392.

[46] M.B. Kgomo, K. Shingange, H.C. Swart, G.H. Mhlongo, Evolution of In_2O_3 morphology from belt to fibrous-like structure for ethanol detection at low working temperature induced by Cr-addition", Appl. Surf. Sci. 639 (2023) 158210 https://doi.org/10.1016/j.apsusc.2023.158210.

[47] T. Aoki, M. Yamamoto, T. Tanabe, T. Yoshida, Mixed phases of GaOOH/β-Ga_2O_3 and α-Ga_2O_3/β-Ga_2O_3 prepared by high energy ball milling as active photocatalysts for CO_2 reduction with water, N. J. Chem. 46 (7) (2022) 3207–3213, https://doi.org/10.1039/D1NJ05245D.

[48] H.-J. Lin, J.P. Baltrus, H. Gao, Y. Ding, C.-Y. Nam, P. Ohodnicki, P.-X. Gao, Perovskite nanoparticle-sensitized Ga_2O_3 nanorod arrays for CO detection at high temperature, ACS. Appl. Mater. Interfaces. 8 (14) (2016) 8880–8887, https://doi.org/10.1021/acsami.6b01709.

[49] Z. Liu, T. Yamazaki, Y. Shen, T. Kikuta, N. Nakatani, Y. Li, O_2 and CO sensing of Ga_2O_3 multiple nanowire gas sensors, Sens. Actuators B: Chem. 129 (2) (2008) 666–670, https://doi.org/10.1016/j.snb.2007.09.055.

[50] H. Kim, C. Jin, S. An, V. Lee, Fabrication and CO gas-sensing properties of Pt-functionalized Ga_2O_3 nanowires, Ceram. Int. 38 (5) (2012) 3563–3567, https://doi.org/10.1016/j.ceramint.2011.12.072.

[51] T.-F. Weng, M.-S. Ho, C. Sivakumar, B. Balraj, P.-F. Chung, VLS growth of pure and Au decorated β-Ga_2O_3 nanowires for room temperature CO gas sensor and resistive memory applications, Appl. Surf. Sci. 533 (2020) 147476, https://doi.org/10.1016/j.apsusc.2020.147476.

[52] S.T. Tan, c.H. Tan, W.Y. Chong, C.C. Yap, A.A. Umar, R.T. Ginting, H.B. Lee, K. S. Lim, M. Yahaya, M.M. Salleh, Microwave-assisted hydrolysis preparation of highly crystalline ZnO nanorod array for room temperature photoluminescence-based CO gas sensor, Sens. Actuators B: Chem. 227 (2016) 304–312, https://doi.org/10.1016/j.snb.2015.12.058.

[53] Y. Zeng, L. Qiao, Y. Bing, M. Wen, B. Zou, W. Zheng, T. Zhang, G. Zou, Development of microstructure CO sensor based on hierarchically porous ZnO nanosheet thin films, Sens. Actuators B: Chem. 173 (2012) 897–902, https://doi.org/10.1016/j.snb.2012.05.090.

[54] K. Wang, T. Zhao, G. Lian, Q. Yu, C. Luan, Q. Wang, D. Cui, Room temperature CO sensor fabricated from Pt-loaded SnO_2 porous nanosolid, Sens. Actuators B: Chem. 184 (2013) 33–39, https://doi.org/10.1016/j.snb.2013.04.054.

[55] I.A. Al-Homoudi, J.S. Thakur, R. Naik, G.W. Auner, G. Newaz, Anatase TiO_2 films-based CO gas sensor: film thickness, substrate and temperature effects, Appl. Surf. Sci. 253 (21) (2007) 8607–8614, https://doi.org/10.1016/j.apsusc.2007.04.068.

[56] Y. Liu, Y. Lei, Pt-CeO_2 nanofibers based high-frequency impedancemetric gas sensor for selective CO and C_3H_8 detection in high-temperature harsh environment, Sens. Actuators B: Chem. 188 (2013) 1141–1147, https://doi.org/10.1016/j.snb.2013.07.069.

[57] J.-K. Choi, I.-S. Hwang, S.-J. Kim, J.-S. Park, S.-S. Park, U. Jeong, Y.C. Kang, J.-H. Lee, Design of selective gas sensors using electrospun Pd-doped SnO_2 hollow nanofibers, Sens. Actuators B: Chem. 150 (1) (2010) 191–199, https://doi.org/10.1016/j.snb.2010.07.013.

[58] H. Liu, J. Zhou, L. Yu, Q. Wang, B. Liu, P. Li, Y. Zhang, High-sensitivity SO_2 gas sensor based on noble metal doped WO_3 nanomaterials, Int. J. Electrochem. Sci. 16 (12) (2021) 211240, https://doi.org/10.20964/2021.12.39.

[59] S.H. Park, S.H. Kim, S.Y. Park, C. Lee, Synthesis and CO gas sensing properties of surface-nitridated Ga_2O_3 nanowires, RSC. Adv. 4 (108) (2014) 63402–63407, https://doi.org/10.1039/C4RA09538C.

[60] A. Afzal, β-Ga_2O_3 nanowires and thin films for metal oxide semiconductor gas sensors: sensing mechanisms and performance enhancement strategies, J. Materiomics 5 (4) (2019) 542–557, https://doi.org/10.1016/j.jmat.2019.08.003.

[61] A. Dey, Semiconductor metal oxide gas sensors: a review, Mater. Sci. Eng.: B 229 (2018) 206–217, https://doi.org/10.1016/j.mseb.2017.12.036.

[62] B. Yang, N.V. Myung, T.-T. Tran, 1D metal oxide semiconductor materials for chemiresistive gas sensors: a review, Adv. Electron. Mater. 7 (2021) 2100271, https://doi.org/10.1002/aelm.202100271.

[63] M. Al-Hashem, S. Akbar, P. Morris, Role of oxygen vacancies in nanostructured metal-oxide gas sensors: a review, Sens. Actuators B: Chem. 301 (2019) 126845, https://doi.org/10.1016/j.snb.2019.126845.